Oceanologia (2015) 57, 318–327

Available online at www.sciencedirect.com

ScienceDirect

journal homepage: www.elsevier.com/locate/oceano

ORIGINAL RESEARCH ARTICLE

Tidal currents in the western Svalbard Fjords☆

Zygmunt Kowalik[a,*], **Aleksey Marchenko**[b], **Dmitry Brazhnikov**[a], **Nataly Marchenko**[b]

[a] *University of Alaska Fairbanks, USA*
[b] *The University Centre in Svalbard, Norway*

Received 4 February 2015; accepted 19 June 2015
Available online 15 July 2015

KEYWORDS
Tides in Svalbard's fjords;
Numerical models;
Observation and model comparison;
Eddy motion and nonlinear effects

Summary The paper is focusing on the tides and on the strong tidal current generated in the western fjords of Svalbard. Numerical model is chosen as a tool to study the barotropic tides. Model results are compared against measured sea level and drifters. Numerical modeling and observation of tides point that the tidal amplitude does not change strongly in these fjords but the tidal currents are enhanced in several locations, namely at the entrance to the Dickson Fjord, in the narrow passages in proximity to Svea, and in the central part of Van Keulenfjorden. As the strongest currents have been found at the passages at Akseløya Island we have focused our research on this location. The narrow northern channel (Akselsundet) at Akseløya is the main waterway to Svea coal mines. Tidal currents computed and observed at the northern tip of Akseløya Island can reach amplitude from 2 to 3 m s^{-1}. Observation of the deployed drifters and calculation of the seeded particles in the passage at Akseløya depicted a complicated pattern of eddies. The jet-like currents and eddies are quite different at the ebb and flood tide phases. As the Akseløya Island orientation relative to the shore is different for the flood and ebb waters the flow through Akselsundet is differently constrained by this geometry. The observations show that the oscillating tidal motion causes large excursions of the water particle. The drifters released in the passage during flood ended up trapped in the eddy on the eastern side of the island.

☆ The authors wish to acknowledge the support of the Research Council of Norway through the SFI project SAMCoT, SIU foundation through the project CPRU-2011/10042 SMIDA.
* Corresponding author at: Institute of Marine Science, University of Alaska Fairbanks, 118 O'Neill, P.O. Box 757220, Fairbanks, AK 99775-7220, USA. Tel.: +1 907 474 7753; fax: +1 907 474 7204.
Peer review under the responsibility of Institute of Oceanology of the Polish Academy of Sciences.

Production and hosting by Elsevier

http://dx.doi.org/10.1016/j.oceano.2015.06.003

1. Introduction

We aim to describe tides and especially tidal currents in the major western fjords of the Svalbard, i.e., in Isfjorden, Van Mijenfjorden, and Van Keulenfjorden. Tidal analysis of the measured sea level at Svea and Longyearbyen (see Fig. 1) describes tidal constituents which are quite similar at both the locations. The dominant tide is semi-diurnal M_2 constituent with amplitude close to 50 cm. The Svea station when compared to Longyearbyen depicts a phase lag of less than 1 h probably due to the constraint in the tide propagation through the narrow straits around Akseløya Island. The main phenomenon which is of interest for the water mixing is the tidal current responsible for the water exchange in the shallow or narrow subdomains. The tide in the domain shown in Fig. 1 will be computed starting from the boundary conditions at the open western boundary along 12°E and the southern boundary along 77°20′N (or 77.33N). The boundary data are based on the computation made by Kowalik and Proshutinsky (1994) and available at the website: http://www.ims.uaf.edu/tide/. For data dissemination, the data were interpolated into a spherical grid with a space resolution of 10 × 10 min (170 × 2160 cells).

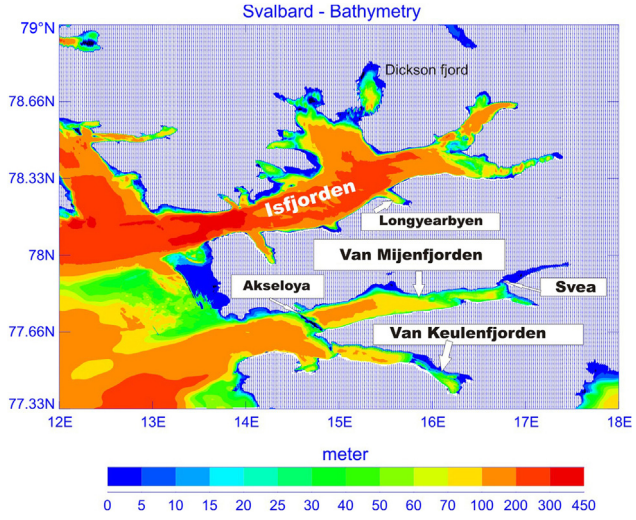

Figure 1 Computational domain, bottom topography, and points where computation or measurements will be of particular interest. Tide gauges are located at Longyearbyen and at Svea.

An example of the tidal chart based on the computation is depicted in Fig. 2. Here amplitude [cm] and phase [degree] for the M_2 constituent are given. As the semidiurnal tide-generating force is very small in the Arctic, the M_2 tide propagates from the Atlantic performing one semidiurnal cycle around the main amphidromic point located in the central Arctic Ocean (Gjevik and Straume, 1989 and also see Fig. 2). Tides around Svalbard are part of this semidiurnal cycle. The change in amplitude and phase is due to Svalbard location between deep Arctic Ocean and shallow Barents Sea.

2. Tidal equations and parameters

To obtain the distribution of tides in the Svalbard Fjords we shall use the vertically averaged equations of motion and continuity in a spherical coordinate system (Gill, 1982):

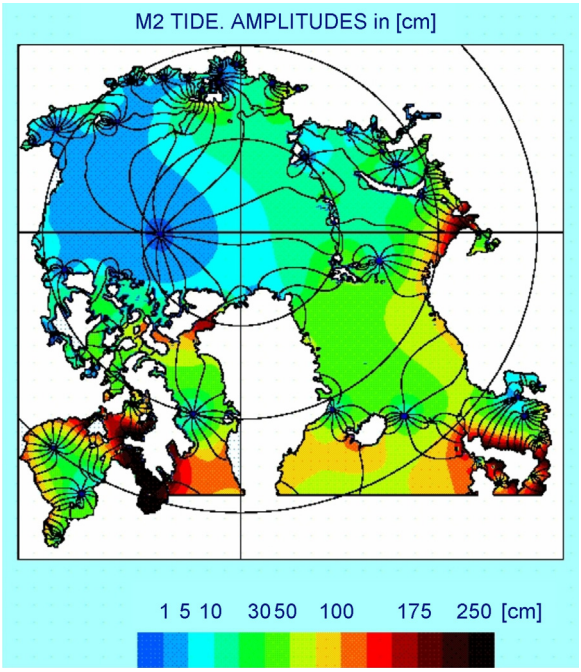

Figure 2 Computed amplitude [cm] of the surface elevation for the semidiurnal constituent M_2 in the Arctic Ocean. Black lines denote phase in degree. Color in proximity to Svalbard indicates amplitude of about 40 cm. (For interpretation of the references to color in this figure legend, the reader is referred to the web version of the article.)

$$\frac{\partial u}{\partial t}+\frac{u}{R\cos\phi}\frac{\partial u}{\partial \lambda}+\frac{v}{R}\frac{\partial u}{\partial \phi}-fv-\frac{uv\sin\phi}{R\cos\phi} = -\frac{g}{R\cos\phi}\frac{\partial}{\partial\lambda}(\alpha\zeta-\beta\zeta_0)-\frac{\tau^b_\lambda}{\rho H}+Au, \tag{1}$$

$$\frac{\partial v}{\partial t}+\frac{u}{R\cos\phi}\frac{\partial v}{\partial \lambda}+\frac{v}{R}\frac{\partial v}{\partial \phi}+fu+\frac{uu\sin\phi}{R\cos\phi} = -\frac{g}{R}\frac{\partial}{\partial\phi}(\alpha\zeta-\beta\zeta_0)-\frac{\tau^b_\phi}{\rho H}+Av, \tag{2}$$

$$\frac{\partial \zeta}{\partial t}+\frac{1}{R\cos\phi}\frac{\partial(Hu)}{\partial\lambda}+\frac{1}{R\cos\phi}\frac{\partial}{\partial\phi}(Hv\cos\phi)=0. \tag{3}$$

The operator A in the horizontal friction term in (1) and (2) is

$$A=N_h\left(\frac{1}{R^2\cos^2\phi}\frac{\partial^2}{\partial\lambda^2}+\frac{1}{R^2\cos\phi}\frac{\partial}{\partial\phi}\left(\cos\phi\frac{\partial}{\partial\phi}\right)\right). \tag{4}$$

The bottom stress components are taken as

$$\tau^b_\lambda=\rho ru\sqrt{u^2+v^2};\qquad \tau^b_\phi=\rho rv\sqrt{u^2+v^2}. \tag{5}$$

In (5) r denotes the bottom drag coefficient; it will be taken as $r = 2.6\times10^{-3}$. This value was first computed by G. Taylor through the estimate of the tidal energy dissipation in the Irish and Bristol Channels (see Defant, 1961, p. 346).

The following notation has been used in the above equations: λ and ϕ denote longitude and latitude, respectively, t is time, ζ is free surface elevation, u and v are velocity components along longitude and latitude, respectively, ρ is water density, N_h is horizontal eddy viscosity (=2.5 $\times$ 10^6 cm^2 s^{-1}), H denotes depth (it does not include the sea level change), f is the Coriolis parameter, g denotes gravity acceleration, R is the radius of the earth, ζ_0 denotes the equilibrium tide, and α and β are parameters accounting for tidal potential perturbations. The above value of the horizontal eddy viscosity N_h is required to preserve numerical stability and it should reasonably reproduce the horizontal turbulent friction as well. The upper limit of this coefficient (if space and time steps are chosen) is given by the numerical stability requirement (Kowalik and Murty, 1993). For the spatial step of 90 m and time step 1 s the upper limit for N_h = 4 $\times 10^7$ cm^2 s^{-1}. The coefficient has the lower limit as well since in proximity to N_h = 1 $\times 10^5$ cm^2 s^{-1} the numerical scheme is again unstable due to the insufficient dissipation.

Tidal forcing is described in (1) and (2) through the terms which are multiplied by coefficients α and β. These terms include the tide-generating potential, but they also contain various corrections due to earth tide and ocean loading (Kowalik and Luick, 2013; Schwiderski, 1980). Coefficient α defines ocean loading; its value ranges from 0.940 to 0.953 according to Ray and Sanchez (1989). The term $\beta\zeta_0$ includes both the tide-generating potential and correction due to the earth tide. It is usually expressed as (Hendeshott, 1977)

$$\beta\zeta_0 = (1 + k - h)\zeta_0. \tag{6}$$

Here k and h denote Love numbers, which are equal to 0.302 and 0.602, respectively. As we do not expect the tide generation in Svalbard Fjords to have taken place in any other way but through the open boundary, the term $\beta\zeta_0$ is set to zero. In the ensuing computations one additional simplification is introduced. Because the Svalbard Fjords are partly covered by ice in winter and its effect on tides in the shallow water can be important, we consider the ice-free summer condition.

Initially, the dependent variables in the integration domain are taken as zero

$$\zeta(x,y)_{t=0} = 0, \tag{7a}$$

$$u(x,y)_{t=0} = 0, \qquad v(x,y)_{t=0} = 0. \tag{7b}$$

Along the solid boundary we assume a normal component of velocity to be zero.

The model is forced through the open boundary of the domain, and on this boundary the sea level is given as a superposition of harmonic oscillations:

$$\zeta(t) = \sum_{n=1}^{n=N} f_n(t)\zeta_n \cos(\omega_n t - g_n + V_n(t_0) + u_n(t)). \tag{8}$$

Here:

ζ_n is the amplitude of tidal constituent ("harmonic") n,
ω_n is the frequency of harmonic n,
$V_n(t_0)$ is the phase of the reference signal of ω_n at time t_0,
g_n is the UT (universal time) phase lag of harmonic n with respect to the Greenwich longitude,
$f_n(t)$ and $u_n(t)$ are the "nodal factor" and "nodal phase" used to adjust the amplitude and phase of the reference signal for nodal changes (18.6 years), respectively,
t_0 is a reference time usually chosen to be immediately prior to the predictions required.

It is convenient to choose 0000 h UT on the first day of predictions. The amplitudes and phases of the tidal constants are taken from Kowalik and Proshutinsky (1994) for the five waves, namely: M_2, S_2, N_2, K_1, and O_1. The computations of the mixed tides were carried out for a 2-month period. After 1 month the full energy of the system became stationary. During the second-month period the sea level and velocity were recorded every hour for further harmonic analysis.

3. Comparison with the sea level measurements

The long-period sea level measurements at Svea and Longyearbyen (see Fig. 1) were reported by Caline (2009). Based on the main tidal constituents for Longyearbyen the prediction is made for the one-month period from May 12 to June 12, 2008 (Fig. 3). The upper panel compares original sea level record (green color) with predicted tides. In the lower panel the residual sea level is plotted. Aside from a few storm surges the residual sea level is related to the nonlinear tides located in proximity to the 4-h periods, i.e., M_6, $2MN_6$, and $2MS_6$.

The computation made with the numerical model, based on the horizontal space resolution of 3 arc second ($\simeq$93 m) along N—S and 15 arc second (appr. 97 m at 78°) along E—W, is compared for the same period with the predicted tides

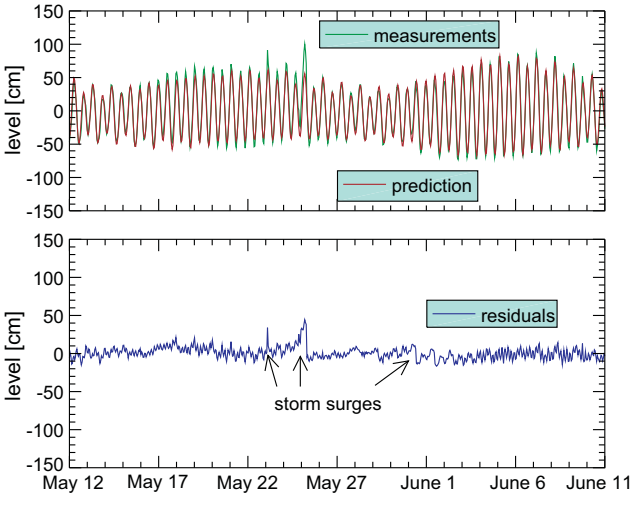

Figure 3 The sea level from May 12 to June 12, 2008 at Longyearbyen, Svalbard. Upper panel. Green color: measurements, brown color: prediction. Lower panel: residuals. (For interpretation of the references to color in this figure legend, the reader is referred to the web version of the article.)

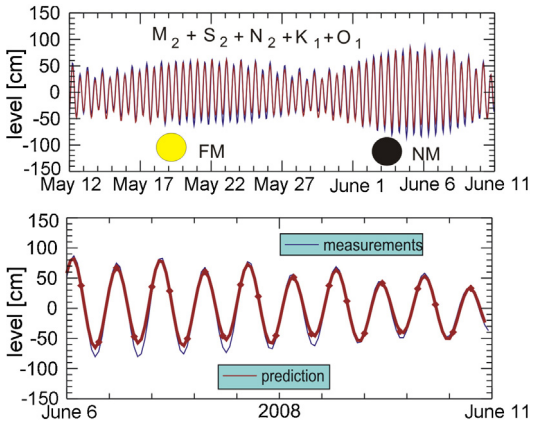

Figure 4 The sea level from May 12 to June 12, 2008 at Longyearbyen, Svalbard. Blue color: measurements, red color: numerical model computation. Lower panel: detail for the shorter period. (For interpretation of the references to color in this figure legend, the reader is referred to the web version of the article.)

(Fig. 4). Upper panel shows comparison for one month and the detailed plot in the lower panel compares 5-day period. Although both panels show that the overall comparison is good the model is predicting slightly lower amplitudes. The model is using only five tidal constituents; the reason for this discrepancy is probably related to the small number of tidal constituents used at the open boundary.

As mentioned, the tides at Svea located at the head of Van Mijenfjorden are not very different from the Longyearbyen located at the middle of Isfjorden. Observations and computations indicate the phase lag between two locations mostly generated by the narrow passages at Akseløya Island. To confirm these observations only M_2 tide is considered at the open boundary and computations are carried out until oscillations are stationary in time. The result for the Svea and Longyearbyen is given in Fig. 5, upper panel. Amplitudes are quite similar and the small phase lag has been generated as well. In the lower panel the sea level depicted at the points located on western (outside) and eastern sides (inside) of Akseløya Island. As these points are located on the different

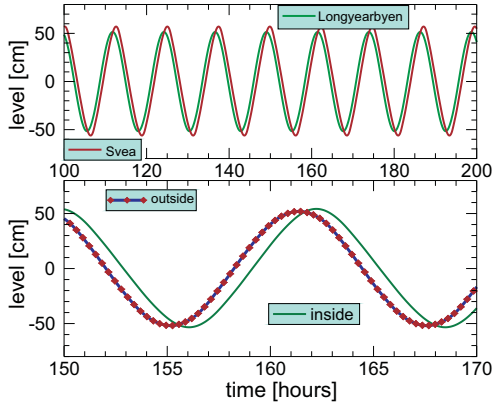

Figure 5 M_2 tide computed by numerical model. Upper panel: sea level at Svea and Longyearbyen. Lower panel: sea level on the western (outside) and eastern (inside) sides of Akseløya Island.

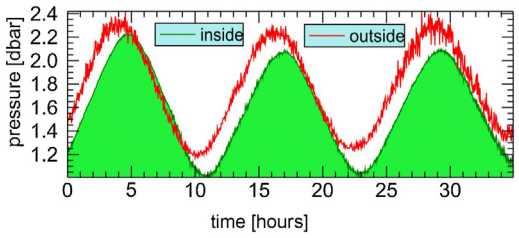

Figure 6 Sea level measured on two sides of Akseløya Island. Outside location is on the western side and inside is on the eastern side. Zero hour denotes 13 h on September 24, 2013.

sides of the Island, the generation of the phase lag is obviously related to the narrow passages at this island. The phase lag between sea levels at two points is slightly variable in time and ranges from 30 to 50 min.

The measurements of the pressure on the two sides of Akseløya Island were performed on May 5–6, 2010 (Marchenko et al., 2011) when the Van Mijenfjorden was covered by sea ice. Data obtained in the ice free season on September 24 and 25, 2013 are given in Fig. 6. The measurements taken in summer and winter confirm well that the phase difference is varying from 0.5 h to 1 h.

4. Tidal currents at flood and ebb

Tidal currents computed at the flood and ebb on June 7, 2008 are given in Figs. 7 and 8 for the entire computational domain. The broad areas in Figs. 7 and 8 show rather small currents in the range of 2 to 10 cm s^{-1}. The large scale figures actually depict only every 15th current vector as plotting vectors in every grid-point will make figure unreadable. The stronger currents are confined to the narrow and shallow passages: at the entrance to the Dickson fjord, at the northern and southern passages at Akseløya Island, in the central part of Van Keulenfjorden, and in the narrow passages in

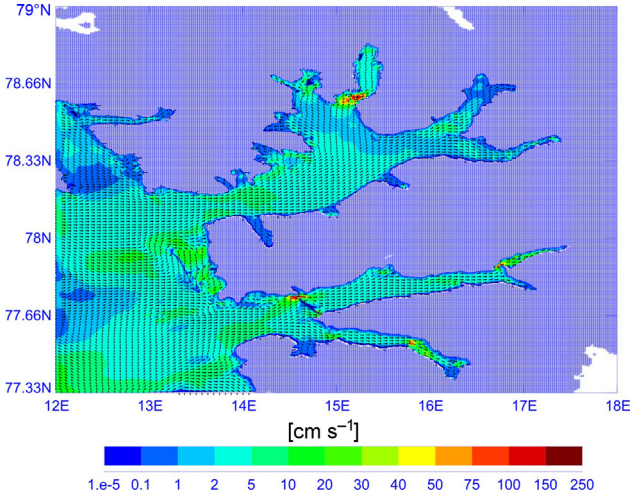

Figure 7 Flood tidal current computed by numerical model. Vectors define direction and colors depict the magnitude in cm s^{-1}. (For interpretation of the references to color in this figure legend, the reader is referred to the web version of the article.)

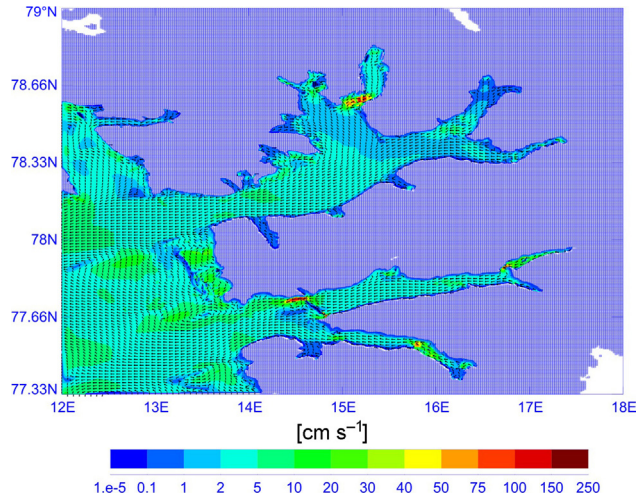

Figure 8 Ebb tidal current computed by numerical model. Vectors define direction and colors depict the magnitude in cm s^{-1}. (For interpretation of the references to color in this figure legend, the reader is referred to the web version of the article.)

proximity to Svea. Currents at northern tip of Akseløya Island reach amplitude from 2 to 3 m s^{-1}. It is of interest to notice that even in these large scale figures at Akseløya Island the ebb currents depict larger pattern when compared against the flood currents. These strong currents play important role in the transport of sediments and ice, in the water mixing, and in navigation through Akselsundet.

5. High resolution tides in the Akseløya Island region

The high spatial resolution (grid size is close to 90 m) used in the present calculations allows to investigate strong currents and fine scale eddies organized in the vicinity of the island. In Fig. 9a and b it is actually impossible to depict every computational grid-point, and the data from every 5th grid point are used. Strong currents are marked by the red and brown colors. The strong jet-like current of up to 250 cm s^{-1} is generated in the northern (main) passage. Ebb and flood currents encounter very different geometry of the fjord's shore and Akseløya Island. On the western side of the passage, the Akseløya Island orientation relative to the shore generated an obtuse angle, as the flood waters are not strongly constrained by this geometry, therefore the flow through the passage does not take all the incoming waters. The part of the flow is deflected to the northern shore and backward to the west resulting in the large sluggish eddy. At the same time at the eastern side of the passage the compact eddy is generated by the incoming flood flow. The eddy's shape and strength is defined by the influence of the Akseløya Island orientation relative to the shore.

The ebb flow (Fig. 9b) on the eastern side of the passage due to acute angle between Akseløya and the fjord's shore shows the strong current acceleration. The ebb jet-like current impinges on the water at the western side of the passage which results in the large domain of the enhanced currents. These currents generate eddy to the south of the main flow. (Regular jet is associated with two eddies but the eddy at the northern side is damped by the shore.) Fig. 9b actually shows two aspects of the jet—eddy interaction, namely that on the one hand this large eddy is spawned by the jet but on the other hand the eddy is feeding the main jet as well. The influence of the Akseløya Island orientation relative to the shore is seen well when the areas of the enhanced current is compared for the flood/ebb patterns (Fig. 9a and b). Thus the current running through the northern passage shows the bimodal character for the flood/ebb tidal streams with the stronger ebb currents on the western side of the passage. An interesting feature of these modeled

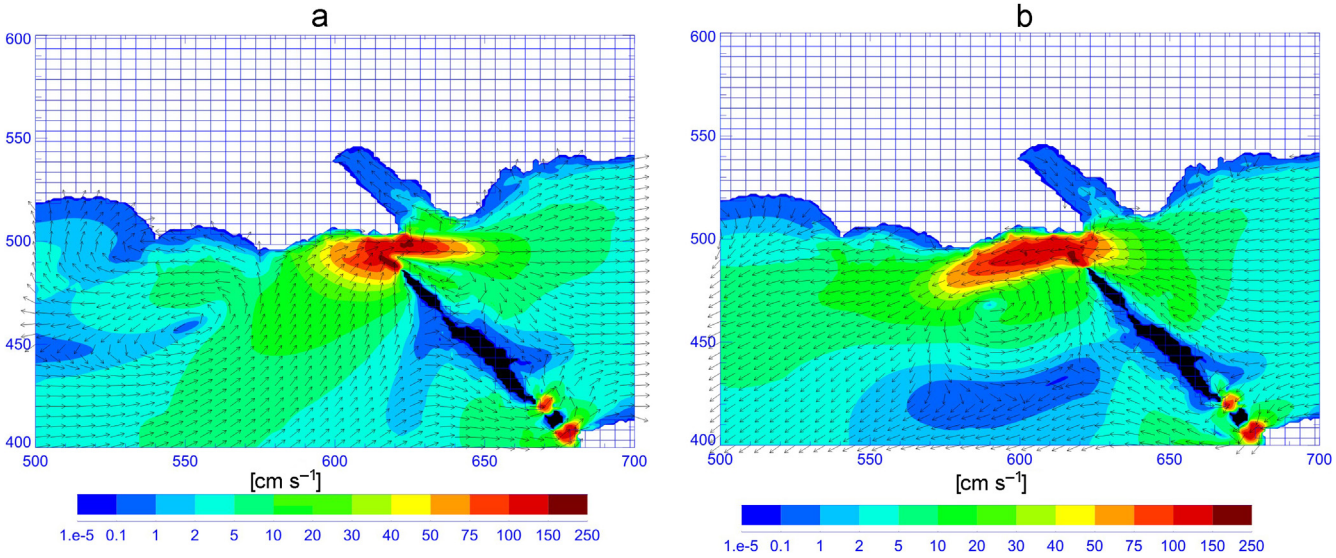

Figure 9 (a) Flood currents in the Akseløya Island region. Vectors define direction and colors depict the magnitude in cm s^{-1}. Distances are given in numerical grid points. (b) Ebb currents in the Akseløya Island region. Vectors define direction and colors depict the magnitude in cm s^{-1}. Distances are given in numerical grid points. (For interpretation of the references to color in this figure legend, the reader is referred to the web version of the article.)

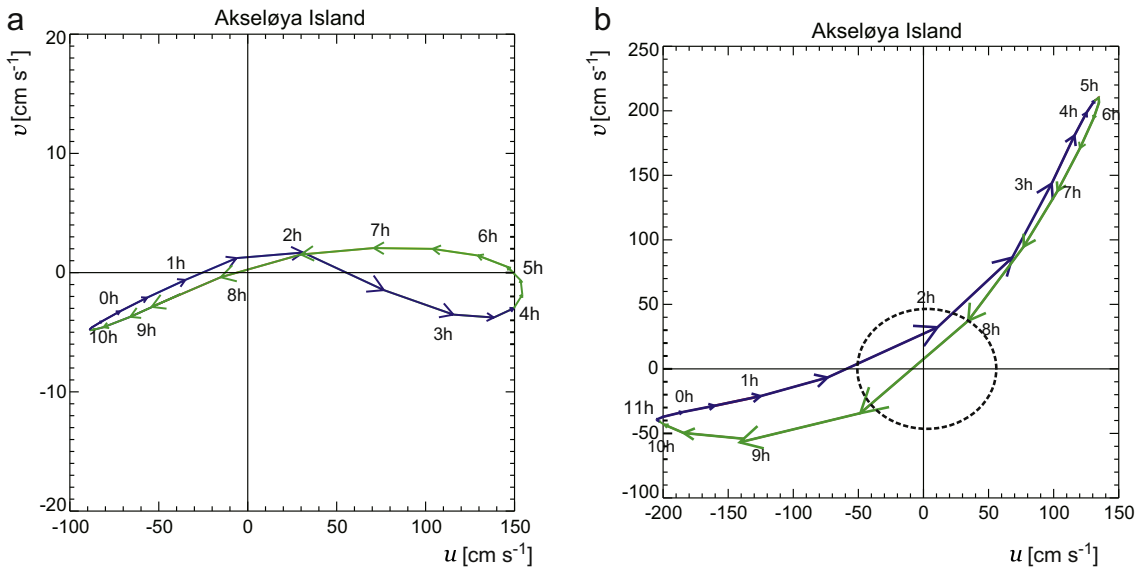

Figure 10 (a) Progressive vector diagram (hodograph) for the 12-h time span at the points 625 along E—W and 500 along N—S, see Fig. 9a. Velocity vectors are plotted from the fixed point with $u = 0$, $v = 0$. The plot connects the variable end of the velocity vectors thus defining the rotation and change of velocity in time. (b) Progressive vector diagram (hodograph) for the 12-h time span at the points 618 along E—W and 492 along N—S, see Fig. 9a. Velocity vectors are plotted from the fixed point with $u = 0$, $v = 0$. The plot connects the variable end of the velocity vectors thus defining the rotation and change of velocity in time. Circle depicts velocity of 50 cm s^{-1}.

tidal eddies is the local depression of the water surface at the center of the eddies. Observations made with drifters released in the Akselsundet confirmed that these depressions are organized in the eddies both during ebb and flood phases of tides.

The current behavior in the given location can be described by the progressive vector diagram (hodograph). Plotting the current vector in time in the u, v coordinates and then connecting the ends of the velocity vectors as they proceed in time, the diagram is obtained which is giving the visual representation of the water motion in the tides. (see Fig. 10a and b). In Fig. 10a the point for the progressive vector diagram was chosen in the channel where currents flow along E—W direction is up to 150 cm s^{-1} while N—S direction is limited to 5 cm s^{-1}. Fig. 10b plot is made off the island tip close to location of the current maximum in Fig. 9a and b. Therefore, the latter vector diagram does not depict unidirectional flow since proximity of the island induces currents in both the directions. The practical answers which plots in Fig. 10 can deliver are related to the current magnitude, direction, and its change in time. For example, one can see that the time span when the small currents can be expected (inside 50 cm s^{-1} circle in Fig. 10b) is quite small as it is located from 8 h to 8.5 h and from 1.65 h to 2.15 h. In both figures the progressive vector diagrams are not enclosing the point with coordinates $u = 0$, $v = 0$ which means that the currents are very asymmetrical and probably quite strong residual currents are present as well.

To qualitatively investigate current patterns in vicinity of Akseløya Island, fourteen experiments were made with floating drifters during September 2013. In the northern Akseløya Island passage the experiments revealed the bimodal drift—patterns related to the flood/ebb cycle.

The observations show that the oscillating tidal motion causes large excursions of the water particle, sometimes up to a few kilometers during one period, i.e., the same order of magnitude as the island's length. The drifters released in the passage during flood ended up trapped in the eddy on the eastern side (see Fig. 9 for eddy location). The typical drift—pattern observed for the flood dominated flow is shown in Fig. 11. The observations confirmed well the local depression of the water surface at the center of the eddies on the eastern side of the island.

The very different drifting path is associated with the outflow through the passage, namely the very strong current shown through the numerical modeling pushes drifters to the west beyond the close proximity of the passage and the large number of drifters confirm this pattern. The surface water marked by drifters travels away from the passage and rarely returns back to the passage, see Fig. 12.

To calculate the Lagrangian velocity a water particle can be seen at point $\vec{r}_0$ at time $t = t_0$ and the change in position at the moment $t = t_1$ can be observed. Assuming the new position of the water particle as $\vec{r}_0 + d\vec{r}$, the velocity of the particle can be defined (up to the first order of approximation), as

$$\frac{d\vec{r}}{dt} = \vec{u}(\vec{r}, t) = \vec{u}(\vec{r}_0, t) + \frac{\partial \vec{u}}{\partial \vec{r}} \cdot d\vec{r}. \tag{9}$$

Because $d\vec{r} = \int_{t_0}^{t_1} \vec{u}(\vec{r}_0)\, dt$, the above formula can be written as,

$$\frac{d\vec{r}}{dt} = \vec{u}(\vec{r}, t) = \vec{u}(\vec{r}_0, t) + \frac{\partial \vec{u}}{\partial \vec{r}} \cdot \int_{t_0}^{t_1} \vec{u}(\vec{r}_0)\, dt. \tag{10}$$

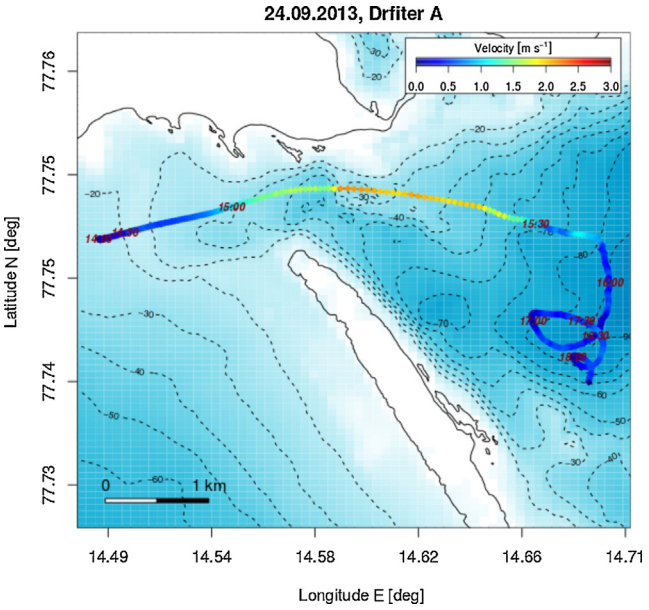

Figure 11 Surface drifter trajectory in the Akseløya Island region measured during flood period. Colors depict the speed in m s^{-1}. Time markers are shown every 0.5 h. (For interpretation of the references to color in this figure legend, the reader is referred to the web version of the article.)

From (10), the Lagrangian velocity is defined as superposition of Eulerian velocity and Stokes velocity, see Longuet-Higgins (1969).

$$\vec{u}_L = \vec{u}_E + \vec{u}_S. \tag{10a}$$

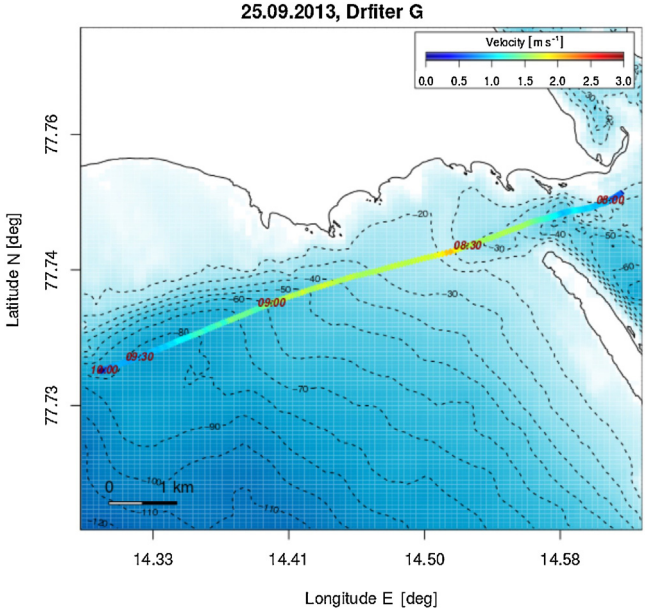

Figure 12 Surface drifter trajectory in the Akseløya Island region measured during ebb period. Colors depict the speed in m s^{-1}. Time markers are shown every 0.5 h. (For interpretation of the references to color in this figure legend, the reader is referred to the web version of the article.)

Here

$$\vec{u}_E = \vec{u}(\vec{r}_0, t) \quad \text{and} \quad \vec{u}_S = \frac{\partial \vec{u}}{\partial \vec{r}} \cdot \int_{t_0}^{t_1} \vec{u}(\vec{r}_0)\, dt.$$

The change in position of specific particle in the horizontal plane follows from (10)

$$dx = u\,dt + 0.5\left(u\frac{\partial u}{\partial x} + v\frac{\partial u}{\partial y}\right)(dt)^2, \tag{11a}$$

$$dy = v\,dt + 0.5\left(u\frac{\partial v}{\partial x} + v\frac{\partial v}{\partial y}\right)(dt)^2. \tag{11b}$$

To depict numerically plausible trajectories a number of particles were released in the numerical grid points close to the northern passage. From the great number of obtained trajectories, two particle trajectories are given to depict the major features related to the flood/ebb currents (Fig. 13). The trajectories often seem to run along the strong E–W current. They seem to follow closed or semiclosed elongated trajectories which do not have similarity to the regular tidal ellipses. The major feature which originates from the big number of particles is again a different behavior of the tidal stream during ebb and flood. Since during ebb period at the western side of the passage the area of the strong currents is much larger than the area of the strong currents during the flood period, the particles during the ebb flow are taken away from the domain of the flood currents. Therefore, the particle migrated during ebb flow to the western side practically will never return to the passage. The particles which are taken through the passage during the flood are located in the tight eddy in the close proximity to the passage. The same particles may eventually find a flow which can transport them to the western side of the passage.

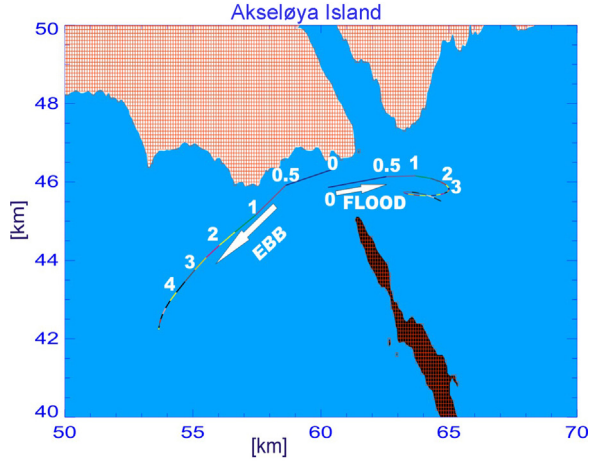

Figure 13 Particle trajectories computed during flood/ebb periods in the Akseløya Island region. Colors define half an hour time steps. Distances are given in km along N–S and E–W. (For interpretation of the references to color in this figure legend, the reader is referred to the web version of the article.)

6. Discussions and conclusions

The main purpose of the present study was to examine tidal currents in the western Svalbard Fjords. Especially important are the strong currents at the Akseløya Island northern passage (Akselsundet), as this is the main navigation route to Svea. The model shows that the lower speed of currents important for the safe passage (lower than 0.5 m s^{-1}) occur approximately for 1–2 h around the maximum or minimum of the sea level. To explain peculiarities of the currents in this passage we have constructed numerical model with the high spatial resolution. The numerical computation and observation testify to the existence of the strong jet-like currents and associated eddies.

Especially interesting is the pattern of interaction of Akseløya Island with the ebb/flood flow. As the island is differently oriented to the ebb and flood flows, the resulting interaction with jet-like currents leads to the different eddies. The strong interaction of the island with the flood flow on the eastern side of the passage modifies the free jet-like current due to the presence of the shear generated by the island. The jet current is deflected toward the island where it spawns the strong eddy. The entire pattern of generation reminds of flow condition which is known as Coanda jet effect (Lalli et al., 2010), i.e. the tendency of a fluid jet to be attracted to a nearby surface. The tidal currents flowing into Van Mijenfjorden and the eddy generated on the flooding tide are quite permanent features which are well confirmed by the satellite observation (Fig. 14). In this image the incoming waters to the Van Mijenfjorden from the Bellsund and surrounding water are laden with different sediment contents which allows them to depict the tidal streams in the Akselsundet. Although we do not consider internal tides in the density stratified water, Støylen and Weber (2010) suggested that when northern passage is covered by the fast ice the barotropic tides may generate internal Kelvin waves which can lead to modification of the water transport described in our paper.

Figure 14 Satellite image of the Akselsundet pointing to the main eddy and associated smaller eddies at the eastern side of the passage. The image was taken on August 24, 2013 at 11:49 UT. Courtesy of Norwegian Polar Institute.

Acknowledgements

We are grateful for logistic support provided by Lars Frode Stangeland and Odd Magne Kvalshagen (UNIS logistic), and Spitsbergen hunter Tommy Sandal.

Appendix A. Simplified model of tides traveling into Van Mijenfjorden

The major changes in the tide pattern caused by the narrow passage of Akselsundet, i.e., velocity enhancement and the phase lag in the tide arrival, can be explained through a simple model of the inlet–bay system as defined by Keulegan (1967). Similar approach was used by Marchenko and Morozov (2013) for the description of tides in the Vallunden Lake connected by narrow strait with the Svea Bay (Van Mijenfjorden). This system consists of channel (Akselsundet) of cross-section E connecting to the bay with surface area S. The change of the sea level (ζ) in the bay is assumed to be uniform over the entire bay, therefore the continuity equation for the inlet-bay system can be written as

$$S\frac{\partial \zeta}{\partial t} = Eu. \tag{A.1}$$

Here E is the cross-sectional area of the entrance, S is the surface area of the bay, and u is the velocity in the inlet. From this simple continuity equation one can conclude that sea level in the bay can be calculated if velocity in the channel is known. The Van Mijenfjorden is considered as water reservoir connected by narrow channel (Akselsundet) with the Bellsund Bay (Fig. 15). Periodical influx of the water in and out of the Van Mijenfjorden is supported by the semidiurnal tide. The geometry taken in our calculation is given in Fig. 15. The channel (inlet) representing Akselsundet on the eastern side is widening toward the Van Mijenfjorden. It actually increases in the width from 1km at the left (L) side to 2 km at the right (R) side while the depth changes from 40 m to 60 m. The length of the channel is 1km. The tide distribution from observations is taken as the boundary condition for the channel in the narrow location (L) of the passage. To find currents in the channel, the equations of mass and momentum balance are written in the following form

$$\frac{\partial \zeta}{\partial t} + \frac{1}{W}\frac{\partial}{\partial x}(uHW) = 0, \tag{A.2}$$

$$\frac{\partial u}{\partial t} + u\frac{\partial u}{\partial x} = -g\frac{\partial \zeta}{\partial x} - ru\frac{|u|}{H}. \tag{A.3}$$

In the above, a rectangular system of coordinates is used. Here the new variable is W; it denotes width of channel. The results of the numerical simulations are illustrated in Fig. 16 for the one-month period. Fig. 16a shows that the variations in the water level at the left (L) and right (R) boundaries of the channel are similar, although the tidal amplitude on the left boundary of the channel is slightly higher.

The phase shift about 0.5 h between tides on the left and right boundaries of the channel (Fig. 16b) has been generated. Fig. 16c shows that the highest speed at the left boundary

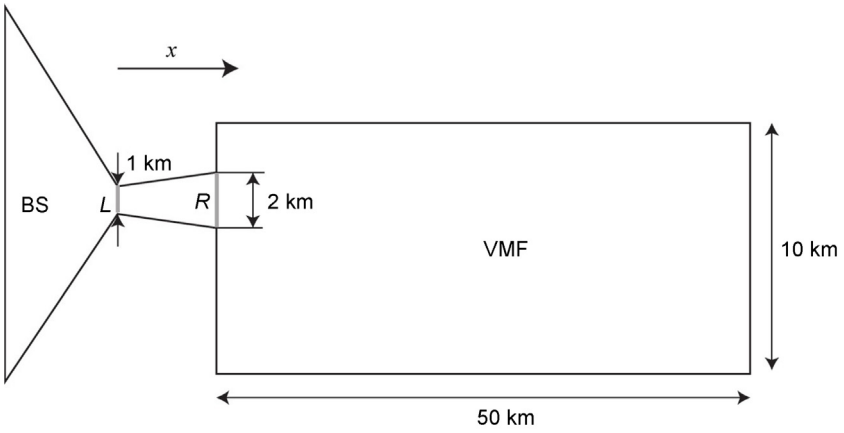

Figure 15 Schematic representation of the geometry in the Aleksundet region. BS stands for the Bellsund and VMF denotes the Van Mijenfjorden. The narrow channel denotes the eastern part of the Akselsundet.

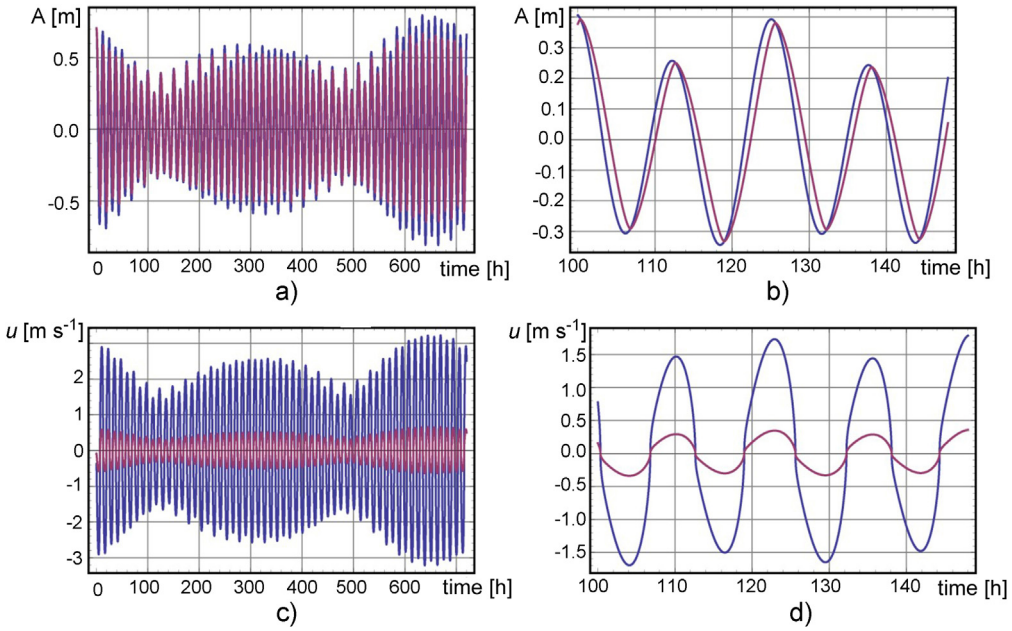

Figure 16 Model calculations of water level over one month (a) and 48 h (b). Model calculations of water velocity over one month (c) and 48 h (d). Blue and purple lines are related to the left (L) and right (R) boundaries of the channel in Fig. 15. (For interpretation of the references to color in this figure legend, the reader is referred to the web version of the article.)

of the channel is close to observed 3 m s^{-1} at the spring tide, while maximum velocity at the right boundary of the channel is close to 0.5 m s^{-1} only. The sea level given for the 2-day period in Fig. 16b shows well phase difference between two locations at the ends of the channel. Fig. 16b for the sea level points that the small speeds are related to the maximum or minimum of sea level over the tidal cycle. Especially important is the timing of the small speeds at the left side of the channel as this is the main navigation route to Svea. The lower speeds (lower than 0.5 m s^{-1}) according to Fig. 16d occur approximately for 1 h around the maximum or minimum of the sea level.

References

Caline, F., 2009. Coastal Sea Ice Conditions Around a Breakwater in a Microtidal, Inner-fjord River Delta in Svalbard (Ph.D. thesis), 221 pp.

Defant, A., 1961. Physical Oceanography, vol. II. Pergamon Press, 598 pp.

Gill, A.E., 1982. Atmosphere—Ocean Dynamics. Academic Press, 662 pp.

Gjevik, B., Straume, T., 1989. Model simulations of the M_2 and the K_1 tide in the Nordic Seas and the Arctic Ocean. Tellus 41, 73—96.

Hendeshott, M.C., 1977. Numerical models of ocean tides. The Sea, vol. 6. John Willey & Sons, New York, 47—96.

Keulegan, G.H., 1967. Tidal flow in entrances: water level fluctuations of basin in communication with seas. Tech. Bull. No. 14. Committee on Tidal Hydraulics, U.S. Army Corps of Engineers, Washington, DC.

Kowalik, Z., Luick, J., 2013. The Oceanography of Tides. https://www.sfos.uaf.edu/directory/faculty/kowalik/Tide_Book/tide_book.pdf.

Kowalik, Z., Murty, T.S., 1993. Numerical Modeling of Ocean Dynamics. World Scientific, 481 pp.

Kowalik, Z., Proshutinsky, A.Yu., 1994. The Arctic Ocean Tides. In: The Polar Oceans and Their Role in Shaping the Global Environment, Nansen Centennial Volume, Geoph. Monograph 85. AGU, 137—158.

Lalli, F., Bruschi, A., Lama, R., Liberti, L., Stefania Mandrone, S., Pesarino, V., 2010. Coanda effect in coastal flows. Coast. Eng. 57, 278—289.

Longuet-Higgins, M.S., 1969. On the transport of mass by the time-varying ocean currents. Deep Sea Res. 16, 431—447.

Marchenko, A.V., Morozov, E.G., 2013. Asymmetric tide in Lake Vallunden (Spitsbergen). Nonlinear Process. Geophys. 20, 935—944, http://dx.doi.org/10.5194/npg-20-935-2013.

Marchenko, A., Shestov, A., Karulin, A., Morozov, E., Karulina, M., Bogorodsky, P., Muzylev, S., Onishchenko, D., Makshtas, A., 2011. Field studies of sea water and ice properties in Svalbard fjords. In: POAC11-148. Montreal, Canada 13 pp.

Ray, R.D., Sanchez, B.V., 1989. Radial deformation of the earth by oceanic tide loading. NASA Technical Memorandum 100743. 51 pp.

Schwiderski, E.W., 1980. On charting global ocean tides. Rev. Geophys. Space Phys. 18, 243—268.

Støylen, E., Weber, J.E.H., 2010. Mass transport induced by internal Kelvin waves beneath shore-fast ice. J. Geophys. Res. 115, C03022.